HYDROGEN, FUEL CELL & ENERGY STORAGE
ECSI IHFCA IROST

Optimization of Renewable Energy and Hydrogen Production for Residential Load in Alberta: A CFD Study

Md Saidur Rahman | **Hassan Ahmad Jan**
Muhammad Razib Hasan | **Amin Etminan***

Faculty of Engineering and Applied Science, Memorial University of Newfoundland and Labrador, St. John's, Canada
* Corresponding author, Email: aetminan@mun.ca

Article Information

Article Type
Research Article

Article History
Received: *05 Jul 2025*
Revised: *01 Oct 2025*
Accepted: *25 Oct 2025*
Published Online:
28 Oct 2025

Keywords

Electrolysis
Electrode Current Density
Hydrogen Production
Laminar Flow
Renewable Energy

Abstract

Hydrogen, as an energy carrier, can potentially transform future energy systems significantly. However, most current commercial hydrogen production methods are carbon-intensive, contributing to atmospheric emissions. To achieve sustainable development, integrating renewable energy sources into distributed energy systems is crucial. When applied to hydrogen production, these renewable sources can drive significant growth and progress toward a cleaner, more sustainable energy future. This study aims to optimize the use of renewable energy sources in Alberta, focusing on utilizing excess electricity for hydrogen production. The novelty of this research lies in evaluating Alberta's solar and wind energy potential to lower residential electricity costs, while simultaneously harnessing surplus electricity from a hybrid system for green hydrogen production. The optimization results show that combining solar photovoltaic, wind turbines, and grid power can provide electricity at a cost 15% lower than the standard grid price. Additional financial key performance indicators, such as net present cost, return on investment, and internal rate of return, further validate the feasibility of this approach for Alberta's residential electricity sector. Water electrolysis, a promising method for hydrogen production using renewable energy, is shown to benefit from the optimized model. The results demonstrate that surplus electricity can significantly reduce hydrogen production costs. Numerical analysis of water electrolysis reveals that the hydrogen gas volume fraction can reach up to 0.2 near the electrode surface and at the electrode's top due to gas accumulation and flow rate dynamics. Furthermore, the distance between the electrode and separator plays a crucial role in hydrogen production; increasing this distance significantly reduces hydrogen output. Analyzing the mid-separator current density in the laminar flow regime suggests that maintaining a consistent current density can enhance electrode longevity and ensure stable hydrogen production.

Cite this article: Rahman, M. S., Jan, H. A., Hasan, M. R., Etminan, A. (2025). Optimization of Renewable Energy and Hydrogen Production for Residential Load in Alberta: A CFD Study. DOI: 10.22104/hfe.2025.7296.1335

Publisher: Iranian Research Organization for Science and Technology (IROST)
DOI: 10.22104/hfe.2025.7296.1335

1 Introduction

Fossil fuels remain the dominant energy source, meeting most global energy demand [1]. Their crucial role in human prosperity is evident, as their discovery and utilization currently account for approximately 84% of the world's primary energy supply – a proportion that continues to rise [2]. The consumption of fossil fuels has shown a steady upward trend and is projected to increase further until 2030 [3]. However, the combustion of fossil fuels produces substantial greenhouse gas emissions, significantly contributing to global warming [4]. Elevated concentrations of greenhouse gases (GHGs) in the atmosphere impose significant societal costs, including adverse effects on human health, property damage from flooding, and reduced agricultural productivity [5]. Estimates suggest that particulate air pollution from fossil fuel combustion is responsible for approximately 8.7 million deaths globally each year [6]. Research also indicates that exposing rice crops to high temperatures (e.g., 38 °C) during the grain-filling stage can lead to a reduction in grain weight [7]. To mitigate the impacts of climate change, it is crucial to transition from centralized, fossil fuel-dependent energy systems to decentralized renewable energy sources, while also reducing per capita fossil fuel consumption [8].

Renewable energy sources – including solar, wind, hydro, geothermal, ocean, biomass, and hydrogen – are expected to lead future energy systems due to their socio-economic and environmental benefits [9]. Hydrogen, the most abundant element in the universe, has the highest gravimetric energy density at 143 MJ/kg and a low gaseous density of 0.089 g/L [10]. These unique properties position hydrogen as a key player in the future energy transition [10]. Hydrogen production methods are generally classified into two categories: non-renewable sources (such as steam methane reforming, pyrolysis, coal gasification, and radiolysis) and renewable sources (including biomass gasification, solar, wind, geothermal, and microbial processes) [11].

More than three-quarters of hydrogen production currently depends on non-renewable energy sources [11]. Hydrogen is classified based on its production method. For instance, hydrogen produced via steam methane reforming (SMR) without carbon capture and storage (CCS) is referred to as gray hydrogen [12]. When CCS is integrated into the same process, the resulting hydrogen is known as blue hydrogen [12]. Hydrogen generated through electrolysis using renewable energy sources is classified as green hydrogen [12]. In the global hydrogen market, electrolysis accounts for only 4% of total hydrogen production, while the majority is derived from non-renewable sources, primarily through SMR [13]. Table 1 summarizes the costs, advantages, and disadvantages of each hydrogen production method.

The SMR and coal gasification remain cost-effective hydrogen production methods due to their relatively low costs. However, their significant carbon emissions make them less favorable from an environmental standpoint. In contrast, renewable-based approaches – such as solar, wind, and geothermal energy – offer cleaner alternatives with substantially lower carbon emissions. Despite these advantages, renewable methods often involve higher initial costs and face challenges in scaling up to meet large-scale hydrogen demand due to factors such as intermittency, geographical constraints, and resource dependency. Table 1 highlights the inherent trade-off between cost-effectiveness and environmental sustainability when selecting a hydrogen production method. Additionally, the data presented in Table 1 demonstrates a strong correlation between Alberta's abundant solar and wind resources and the feasibility of using water electrolysis for green hydrogen production. Given the availability of these renewable energy sources, they provide a reliable and sustainable power supply for electrolysis, making it the preferred method for hydrogen production in this study.

Water electrolysis powered by renewable energy sources is a promising method for green hydrogen production and has attracted significant research interest [12]. In remote regions rich in renewable energy sources such as wind and solar, electrolysis offers an opportunity to produce hydrogen on a smaller scale to meet various energy needs [14]. These applications include powering light manufacturing industries and serving as a solution for electricity peak shaving, whether integrated with the grid or operating independently [14]. During electrolysis, reduction occurs at the cathode, where hydrogen is collected, while oxidation takes place at the anode, where oxygen is gathered [10]. At maximum conversion efficiency, water electrolysis requires 39.4 kWh of energy to produce 1 kg of hydrogen [15]. However, most commercial electrolyzers consume approximately 50 kWh per kg of hydrogen produced [15].

Two well-established electrolysis technologies are alkaline water electrolysis and proton exchange membrane (PEM) electrolysis. In alkaline water electrolysis, a highly corrosive electrolyte, such as sodium hydroxide (NaOH) or potassium hydroxide (KOH), is used, with a pH ranging from 13 to 14 [16]. The anode and cathode are separated by an ion exchange membrane. This method has a relatively low efficiency of 60–70%, with a current density ranging from 0.2 to 0.4 $\mathrm{A/cm^2}$ [16]. In contrast, PEM electrolysis achieves an efficiency of 80% and operates at a higher current density of 1.6 $\mathrm{A/cm^2}$ [12]. The highest efficiency, exceeding

90%, is observed in solid oxide electrolysis; however, this technology is not yet commercially available [16]. During conventional water electrolysis, gas bubbles – being non-conductive – adhere to the electrodes, reducing their exposure to the electrolyte. This increases system resistance, leading to energy losses [17]. In a capillary-fed electrolyzer, the PEM is replaced by a porous hydrophilic separator, with the electrolyte positioned at the bottom of the device, improving system performance [17].

Table 1. Different hydrogen production methods, costs, benefits and challenges

Sources	Cost (\$/kg H_2)	Pros	Cons	Connection to Current Research
Steam methane reforming (SMR)	0.9-3.2 [11]	Generates the highest yield of hydrogen and is a cost-effective method [11]	Emissions reach 9.35 kg CO_2/kg of H_2 production [18]	Highlights the necessity of shifting towards renewable energy solutions as part of decarbonization efforts.
Coal gasification	1.2-2.2 [11]	Meets 18% of global hydrogen demand and economical method for regions with abundant coal reserves [19]	Less efficient (60-75%) compared to SMR (70-85%), additionally it emits more than twice the amount of emissions than SMR [19]	Demonstrates the limitations of fossil fuel-based methods compared to cleaner renewable energy solutions.
Radiolysis	3.18-6.17 [20]	High-capacity factor (90%), low carbon footprint (0.43 kg CO_2/kg H_2) [21]	The fundamental disparity of safety strategies between the nuclear facility and H_2 production [21]	Could benefit from CFD modeling to enhance efficiency but is less aligned with Alberta's solar and wind resources.
Biomass gasification	1.25-2.20 [22]	CO_2 released during the process is offset by the carbon dioxide absorbed by plants during their growth [22]	Low rates of H_2 production and reaction depends on steam-biomass ratio, catalyst, and temperature [22]	Relevant to Alberta's agricultural sector but less focused on optimizing solar and wind energy for residential use.
Solar	0.98-6.02 [23]	Green hydrogen production with sustainable energy sources and large-scale infrastructure would reduce the levelized cost of hydrogen [24]	Lower efficiency of solar cells, intermittency, and variations in solar energy intensity depending on location [11]	Highly relevant, focusing on solar energy integration for hydrogen production in Alberta's residential sector.
Wind	2.27-2.70 [23]	Green hydrogen production with sustainable energy sources and large-scale infrastructure would reduce the levelized cost of hydrogen [24]	Intermittency and location of the system would create difficulties in harnessing renewable energy [24]	Directly relevant, focusing on wind energy integration for hydrogen production in Alberta's residential energy systems.
Geothermal	1.44 [25]	A combined geothermal-assisted hydrogen liquefaction plant has the potential to reduce the levelized cost of hydrogen, presenting a highly promising opportunity [25]	However, geothermal energy has global warming potential [26]	Less relevant than solar and wind in the residential context.
Microbial process	2.13 [22]	Low operating cost and less energy-intensive [22]	Need sunlight and the presence of O_2 reduces hydrogen production [11]	Limited relevance to residential applications compared to solar and wind energy systems.

In a capillary-fed electrolyzer, the electrodes maintain direct contact with the electrolyte on the inner side through the separator's capillary action, while the outer side remains dry [17]. This design prevents bubble formation on the electrode surface, significantly reducing system resistance [17]. The International Renewable Energy Agency (IRENA) has set a target to lower cell energy consumption to below 42 kWh per kilogram of hydrogen by 2050 [17]. The capillary-fed electrolyzer has demonstrated an efficiency of 98%, achieving a current density of $0.5\,\mathrm{A/cm^2}$ with an energy consumption of 40.4 kWh/kg of hydrogen produced [17]. Advancements in industrial electrochemical engineering and electrolyzer technology indicate that alkaline water electrolysis remains the preferred method for large-scale hydrogen production [27].

This study aims to evaluate the integration of hybrid energy systems in residential settings and explore the utilization of surplus electrical energy to enhance green hydrogen production. Notably, it is the first reported analysis and optimization effort conducted in Medicine Hat, Alberta, a location with substantial solar and wind energy potential. Previous research has not directly examined the use of hybrid energy systems in the residential sector to reduce the levelized cost of electricity (LCOE) while utilizing excess electricity for green hydrogen production. The primary objective of this study is to assess the effectiveness of harnessing surplus energy from hybrid systems to lower hydrogen production costs. By identifying the hybrid system with the lowest LCOE, hydrogen production expenses can be further minimized. Additionally, computational fluid dynamics (CFD) modeling of hydrogen production is expected to offer valuable insights, particularly regarding electrode longevity. Enhancing electrode durability could significantly reduce future operational costs of electrolyzers, thereby contributing to a reduction in the overall cost of hydrogen production.

2 Methodology

Various simulation tools can be employed to assess the feasibility of renewable energy systems from technical, economic, and environmental perspectives [28]. HOMER Pro software is widely used for optimizing microgrid designs across different sectors, including rural areas, island communities, military installations, and grid-connected buildings. It evaluates both engineering and economic factors, enabling comparisons with baseline configurations [28]. HOMER Pro can optimize hybrid energy systems that integrate solar, wind, utility loads, and battery storage. Additionally, it also facilitates sensitivity analysis based on net present cost (NPC), operating costs, and emissions [29]. A higher renewable fraction, combined with a lower LCOE, indicates that a greater share of the total energy is sourced from renewables while maintaining a reduced electricity cost per unit [30]. In general, systems with lower LCOE contribute to reducing hydrogen production costs when water electrolysis is utilized [31]. Although hydrogen production from non-renewable sources remains more cost-effective than electrolysis [32], surplus electricity from renewable sources can make electrolysis-based hydrogen production economically viable [32].

Computational fluid dynamics is a powerful tool for simulating hydrogen production, providing insights into thermal, electrochemical, and fluid phenomena within electrolyzer cells [33]. The performance of an electrolyzer is typically evaluated using a polarization curve under different operating conditions, offering a detailed understanding of the system's behavior [33]. For proton exchange membrane (PEM) electrolysis, the optimal operating temperature ranges from 313 K to 353 K [34], whereas alkaline water electrolysis operates most efficiently between 323 K and 343 K with an electrolyte concentration of 32% KOH by weight [33]. Increasing the operating temperature can enhance current density in alkaline electrolysis [35]. However, high-temperature electrolysis presents challenges, such as the need for a pressurized operation to manage saturated water vapor and ensure the safety and stability of system components. CFD modeling is an effective tool for identifying system characteristics, optimizing alkaline electrolysis design, and streamlining sensitivity evaluations while reducing assessment costs [35]. It enables a comprehensive fluid flow and membrane properties analysis, which is often more efficient than experimental approaches [36]. Key parameters such as electrode-diaphragm gap, temperature, diaphragm porosity, and width significantly influence current density, and CFD provides a more detailed understanding of their effects compared to experimental methods [37].

2.1 System description

This research established a system setup in Medicine Hat, Alberta, Canada. Solar irradiation data was collected from pvwatts.nrel.gov, while wind velocity data was retrieved from climate.weather.gc.ca. These data points and annual residential load information were used as inputs in HOMER Pro to conduct a feasibility analysis. The analysis evaluated the potential of grid power, wind energy, and solar PV systems as primary energy sources. The system schematic is shown in Figure 1. Grid and wind power were connected to the AC busbar, whereas solar PV was connected to the DC busbar. A system converter was incorporated for DC/AC conversion. The wind turbine model selected AWS HC

1.8 kW and the cut-in and cut-out speeds are 2.2 and 12 m/s, respectively. For solar PV, the Canadian Solar Superpower CS6K-295MS model, with a capacity of 5 kW and 18.02% efficiency, was chosen. The system converter selected was the Studer AJ 1000-12, with a capacity of 3.5 kW. All components were sourced from the HOMER Pro library.

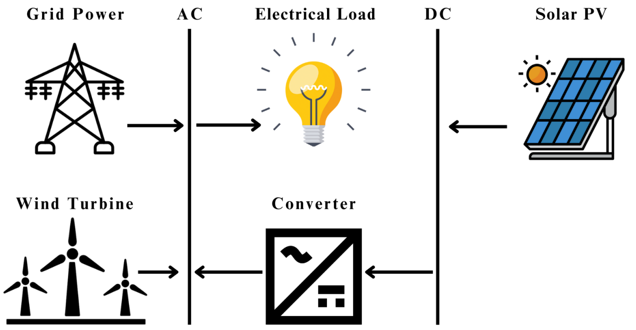

Fig. 1. Schematic of the hybrid system.

This research established a system setup in Medicine Hat, Alberta, Canada, integrating solar and wind energy sources. Solar irradiation data was obtained from pvwatts.nrel.gov, while wind velocity data was sourced from climate.weather.gc.ca. These datasets, along with annual residential load profiles, were used as inputs in HOMER Pro a feasibility analysis. The study assessed grid power, wind energy, and solar photovoltaic systems as primary energy sources. As shown in Figure 1, the system configuration connected the grid and wind power to the AC busbar, while the solar PV system was linked to the DC busbar. A system converter was included to facilitate DC/AC conversion. For component selection:

- Wind turbine: AWS HC 1.8 kW model with a cut-in speed of 2.2 m/s and a cut-out speed of 12 m/s.
- Solar PV: Canadian Solar Superpower CS6K-295MS model with a 5 kW capacity and 18.02% efficiency (flat plate design).
- System converter: Studer AJ 1000-12 with a 3.5 kW capacity.

All components were selected from the HOMER Pro library to ensure compatibility and accurate performance evaluation.

The seasonal residential load profile, illustrated in Figure 2, indicates that the maximum load occurred in June, with an upward trend observed during the winter months. For the sensitivity analysis in HOMER Pro, several key parameters were selected:

- Grid electricity price: Considered at \$0.143/kWh and \$0.150/kWh to account for potential price fluctuations.
- Capital cost multiplier: A 20% increase in cost was applied to the wind turbine, solar PV, and system converter to assess economic sensitivity.

These parameters were chosen due to the inherent variability in grid electricity prices, which are influenced by market dynamics and regulatory policies at both federal and provincial levels. Similarly, capital costs fluctuate due to global market trends and inflation, making them critical factors in evaluating the system's economic resilience under different conditions.

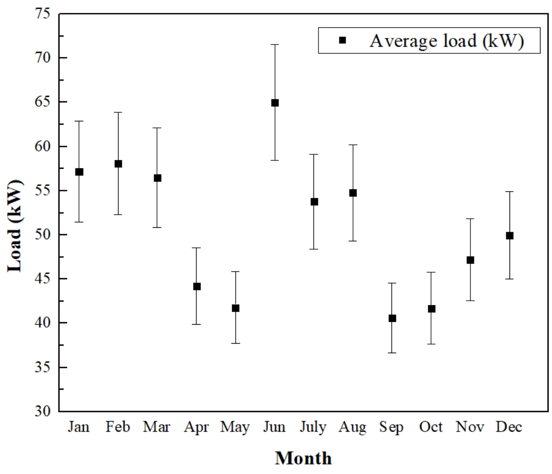

Fig. 2. Seasonal residential load profile.

Figure 3 illustrates the monthly average solar irradiation in Medicine Hat, Alberta, Canada, with the maximum irradiation occurring during the summer months (May-July). Figures 3 to 5 were generated using our in-house Python code. Solar irradiation reached its highest levels in the summer, followed by a gradual decline in fall and spring, and a sharp decrease in winter. During the summer, solar irradiation ranged between 6.14 and 7.33 kWh/m^2/day, with peak levels occurring in July. This variation reflects seasonal changes in solar energy availability, with July experiencing the highest solar intensity due to longer daylight hours and more direct sunlight. In the fall, irradiation values ranged from 3.33 to 6.63 kWh/m^2/day. In the spring, irradiation began to rise again, fluctuating between 2.59 and 5.59 kWh/m^2/day. During the winter season, solar irradiation ranged from 1.68 to 1.90 kWh/m^2/day, with the lowest levels recorded in December. This reduction insolar energy availability in winter is typical due to shorter daylight hours and a lower sun angle, resulting in less direct and weaker sunlight. These seasonal variations, particularly the higher irradiation levels in the warmer months, are crucial for compensating for the lower irradiation experienced in winter, thus enhancing the overall annual solar energy potential. The average annual irradiation was 4.38 kWh/m^2/day.

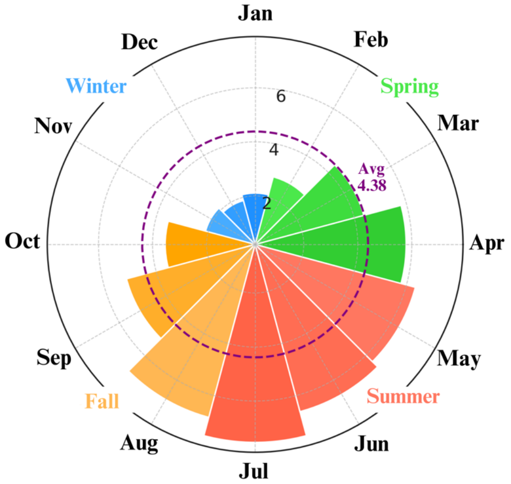

Fig. 3. Sunburst diagram of monthly average solar irradiation.

Figure 4 illustrates the monthly average clearness index, with the highest value recorded in December at 0.79. Throughout the winter, the clearness index ranged from 0.75 to 0.79, indicating relatively clear atmospheric conditions that allow more sunlight to penetrate. In contrast, the clearness index was lowest during the summer, varying between 0.57 and 0.66, reflecting increased cloud cover that reduces solar radiation transmission. During the transitional seasons, the clearness index exhibited moderate values, ranging from 0.71 to 0.73 in the fall and fluctuating between 0.63 and 0.64 in the spring, These seasonal variations are influenced by atmospheric conditions, including cloudiness, humidity, and air pollution, which can significantly affect the availability and quality of solar radiation for solar energy applications. The annual average clearness index was 0.67.

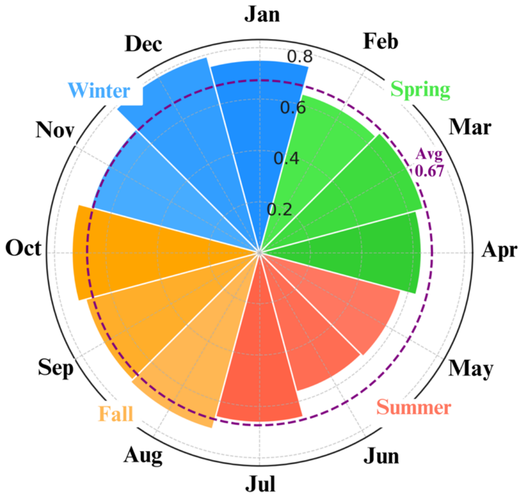

Fig. 4. Sunburst diagram of monthly clearness index.

The monthly average wind velocity is shown in Figure 5. Seasonal analysis revealed that wind speeds were highest in the spring, followed by winter, summer, and fall. During the spring, wind speeds ranged from 3.73 to 4.83 m/s, with the peak recorded in February, suggesting strong air movement during the transition from winter to spring. The elevated wind speeds during this period could be attributed to seasonal shifts in atmospheric pressure patterns and temperature gradients, which enhance wind activity. In winter, wind speeds were slightly lower, ranging from 3.78 to 4.69 m/s. This indicates that while winter experiences relatively strong winds, they are generally less intense than in spring. During the summer, wind speeds decreased further, varying between 3.55 and 4.23 m/s, likely due to more stable atmospheric conditions and less pronounced temperature differences. In fall, wind speeds were the lowest among the seasons, ranging from 3.62 to 3.93 m/s, indicating more stable atmospheric conditions as the season transitioned to winter. Overall, the annual average wind speed was calculated to be 4.07 m/s, indicating a moderate wind resource potential throughout the year. These seasonal variations could influence the optimization of wind energy harvesting strategies. Wind speed is a critical factor in selecting wind turbines, as it significantly impacts their operational performance and economic feasibility.

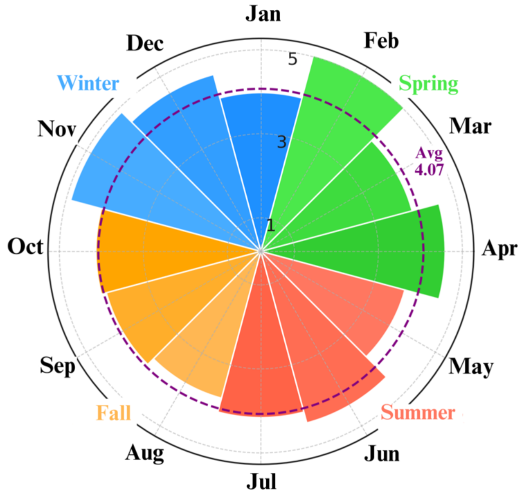

Fig. 5. Sunburst diagram of monthly average wind speed

Using Figure 5, these wind speed values were used to find Rayleigh probability distribution for wind characteristics at this location. The Rayleigh probability distribution was calculated using the following equation [38] and is shown in Figure 6.

$$\phi_u = \frac{\pi v}{2 v_m} \exp\left[-\left(\frac{\pi}{4}\right)\left(\frac{v}{v_m}\right)^2 \right] \tag{1}$$

where ϕ_u is Rayleigh probability distribution, v is wind speed (m/s), and v_m is mean wind speed (m/s).

One year of wind speed data for Medicine Hat, Alberta, was collected from climate.weather.gc.ca, and the mean wind speed was calculated. When the shape parameter in the Weibull probability distribution is set to 2, it forms a Rayleigh distribution [39]. A shape parameter of 2 skews the distribution toward a higher frequency of lower wind speeds, making it suitable for most locations [40]. Figure 6 also shows that most data points are concentrated around the mean wind speed, indicating a peak or higher probability density near the mean value. This suggests that wind speeds near the mean occur more frequently than those farther from it. However, the Rayleigh distribution has limitations when applied to offshore wind probability distributions [39].

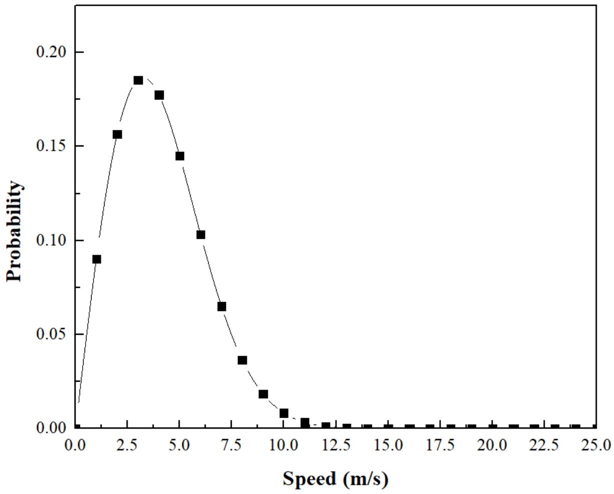

Fig. 6. Rayleigh probability distribution of wind speed.

HOMER Pro uses the following equations to calculate the net present cost and LCOE in the optimization algorithm [41].

$$C_{\mathrm{NPC}} = \frac{C_{\mathrm{ann,tot}}}{\mathrm{CRF}(i, R_{\mathrm{proj}})} \tag{2}$$

where C_{NPC} is net present cost, $C_{\mathrm{ann,tot}}$ is the total annualized cost, i is the annual real interest rate, R_{proj} is project lifetime, and CRF is the Capital recovery factor.

The capital recovery factor can be calculated as

$$\mathrm{CRF}(i, N) = \frac{i(1+i)^N}{(1+i)^N - 1} \tag{3}$$

where, N is the number of years.

$$\mathrm{LCOE} = \frac{C_{\mathrm{ann,tot}}}{E_{\mathrm{prim}} + E_{\mathrm{def}} + E_{\mathrm{Grid,sales}}} \tag{4}$$

where E_{prim} is the total amount of primary load, E_{def} is the total amount of deferrable load, and $E_{\mathrm{Grid,sales}}$ is the amount of energy sold to the grid per year. HOMER's optimization process ranks system configurations by NPC instead of LCOE, as the definition of LCOE is often debated, while NPC is more widely recognized and consistently defined [41].

3 CFD Modeling

3.1 Theoretical description

COMSOL Multiphysics 6.2 was used as the CFD modeling tool. The geometry of the computational domain is shown in Figure 7, with the entire geometry is divided into three compartments: two for the electrodes (cathode and anode) and one for the separator. Hydrogen is collected at the cathode, which has dimensions of 150 mm × 10 mm, while oxygen is collected at the anode, which shares the same dimensions as the cathode. The separator, positioned between the electrodes, measures 150 mm × 2 mm.

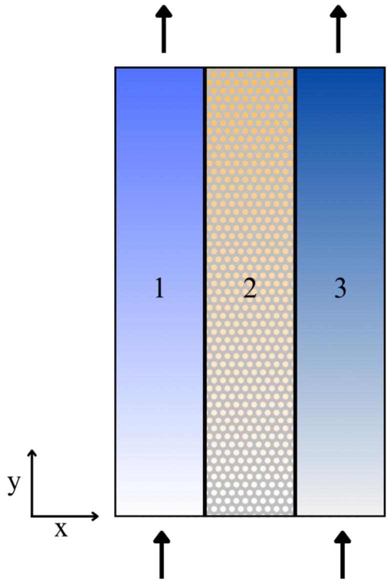

Fig. 7. Modeling geometry (1 = cathode, 2 = separator, 3 = anode).

The potassium hydroxide (KOH) electrolyte was used and fed into the bottom of the compartments, while a biphasic mixture (liquid and gas) was released at the top. The fundamental water electrolysis reaction is shown in the following reactions [42]:

$$2\,\mathrm{H_2O(l)} + 2\,\mathrm{e^-} \longrightarrow \mathrm{H_2(g)} + 2\,\mathrm{OH^-}$$
$$4\,\mathrm{OH^-} \longrightarrow 2\,\mathrm{H_2O(l)} + \mathrm{O_2(g)} + 4\,\mathrm{e^-}$$

In the proposed model, two physics were used to simulate the system: a) water electrolyzer for the polarization curve and b) Euler-Euler model with laminar flow for gas evolution. The Reynolds number for the model was obtained as 1700 (i.e., less than 2100), justifying the selection of the laminar flow model. The polarization curve plays a crucial role in assessing the electrochemical performance of the electrolyzer. Rodríguez and Amores [33] previously utilized the Electric Currents module in COMSOL Multiphysics to model the polarization curve and employed a two-phase turbulent bubbly flow model for gas evolution. The simulation results were validated experimentally, and the effects of temperature and electrode-diaphragm distance were also investigated [33]. Mohsin et al. [43] provided an overview of the flow models for alkaline water electrolysis developed by researchers using CFD, noting that most of these studies focused on turbulence models. This study considered the Euler-Euler model with laminar flow to investigate gas evolution in the laminar flow domain, following a COMSOL Multiphysics report [44]. The governing equations for the conservation of currents in water electrolyzer physics are mentioned in the following [45]:

$$\nabla \cdot i_l = i_{v,\text{tot}} \tag{5}$$

where $i_{v,\text{tot}}$ is volumetric current density. Ohm's law for electrolyte phase:

$$i_l = -\sigma_{l,\text{eff}} \nabla \phi_l \tag{6}$$

where $\sigma_{l,\text{eff}}$ is effective electrical conductivity of the electrolyte. Conservation of current in electrode phase:

$$\nabla \cdot i_s = -i_{v,\text{tot}} \tag{7}$$

Ohm's law for electrode phase:

$$i_s = \sigma_s \nabla \phi_s \tag{8}$$

where i_s is current density in solid, σ_s is electrical conductivity of the solid material. The continuity equation for the continuous and dispersed phases is mentioned in the following [46]:

$$\frac{\partial \phi_c}{\partial t} + \nabla \cdot (\phi_c u_c) = m_{dc} \left(\frac{1}{\rho_c} - \frac{1}{\rho_d} \right) \tag{9}$$

where ϕ_c is the volume fraction of the continuous phase, u_c is the velocity of the continuous phase, ρ_c is density of the continuous phase, ρ_d is the density of the dispersed phase, and mdc is mass transfer between dispersed and continuous phase.

$$\frac{\partial \phi_d}{\partial t} + \nabla \cdot (\phi_d u_d) = -m_{dc} \frac{1}{\rho_d} \tag{10}$$

where ϕ_d is the volume fraction of the dispersed phase, and u_d is the velocity of the dispersed phase. The momentum equation for the continuous and dispersed phases is mentioned in the following [46]:

$$\rho_c \frac{\partial u_c}{\partial t} + \rho_c (u_c \cdot \nabla) u_c = \nabla \cdot (-pI + \tau_c) + \rho_c g + \frac{F_{m,c}}{\phi_c} + F_c + m_{dc}(u_{\text{int}} - u_c) \tag{11}$$

where p is pressure, I is identity matrix, pI is pressure gradient force, τ_c is stress tensor for continuous phase, g is gravitational acceleration, $F_{m,c}$ is external forces, F_c is interaction forces, and uint is interface velocity between phases.

$$\rho_d \frac{\partial u_d}{\partial t} + \rho_d (u_d \cdot \nabla) u_d = \nabla \cdot (-pI + \tau_d) + \rho_d g + \frac{F_{m,d}}{\phi_d} + F_d + m_{dc}(u_{\text{int}} - u_d) \tag{12}$$

where τ_d is the stress tensor for the dispersed phase, and $F_{m,d}$ is external forces on the dispersed phase.

To solve the aforementioned differential equations, the following assumptions were made to ensure convergence and reduce the computational cost of the model: (1) the fluid is Newtonian and incompressible, (2) the flow is laminar, (3) the two phases are at the same pressure, (4) there is no gas crossover through the separator, and (5) the electrolyte is assumed to be well-mixed. The constant, initial, and boundary conditions are listed in Error! Reference source not found. It is noted that all the initial and boundary conditions were applied for the final CFD simulations.

Table 2. Constant, initial, and boundary conditions in the simulation domains

Description	Value
Electrode-separator distance	10 [mm]
Exchange current density, cathode	200 [A/m^2]
Exchange current density, anode	2 [A/m^2]
Average inlet velocity	0.1 [m/s]
Pressure	1 [atm]
Operating temperature	343.15 [K]
Reference temperature	293.15 [K]
Electrolyte concentration	6.1 [mol/m^3]
Cell voltage	1.2 [V]
Separator porosity	0.3
Water molar mass	18 [g/mol]
Hydrogen molar mass	2 [g/mol]
Oxygen molar mass	32 [g/mol]
Hydroxide molar mass	17 [g/mol]
Bubble diameter	60 [μm]

3.2 Mesh independence

Various mesh configurations were assessed to ensure grid independence by comparing the results. The mesh was considered suitable when the variation between successive results remained within 5%. The total number of elements for each configuration was as follows: 56,400 for the coarse mesh (Mesh I), 147,200 for the fine mesh (Mesh II), and 234,000 for the finer mesh (Mesh III). The pressure (Pa) was measured in the middle of the cathode compartment (5 mm) for each mesh, and the results are presented in Figure 8. The difference between the fine and finer mesh configurations was observed to be less than 3.5%. To reduce computational cost while capturing better results and representing the geometry of the problem more accurately, the fine mesh (Mesh II) was selected for the numerical study.

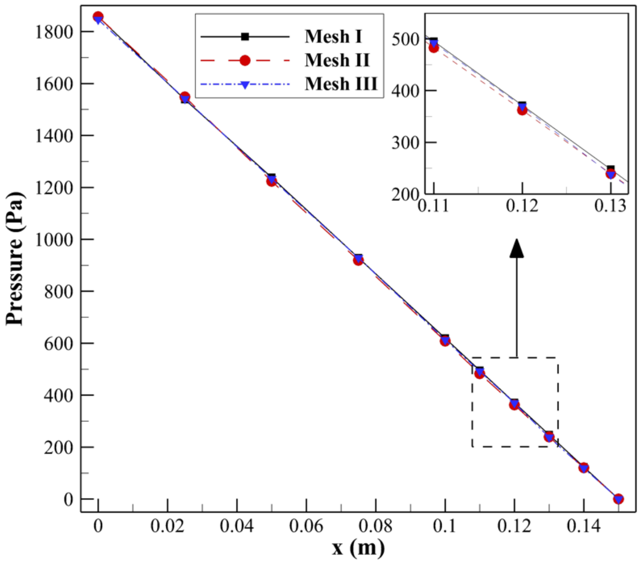

Fig. 8. Mesh independence study.

Figure 9 illustrates the application of a fine mesh within the model. A rectangular mesh configuration was utilized, particularly well-suited for the model's regular geometry. The fine mesh establishes a higher resolution of the computational grid, facilitating more accurate simulations by capturing detailed variations in physical quantities across the domain. This meshing approach is crucial for resolving intricate system features and enhancing the precision of numerical results, particularly in regions with steep gradients or localized phenomena.

Figure 9 illustrates the application of a fine mesh within the model. A rectangular mesh configuration was used, which is particularly well-suited for the model's regular geometry. The fine mesh enhances the resolution of the computational grid, facilitating more accurate simulations by capturing detailed variations in physical quantities across the domain. This approach is essential for resolving intricate system features and improving the precision of numerical results, particularly in regions with steep gradients or localized phenomena.

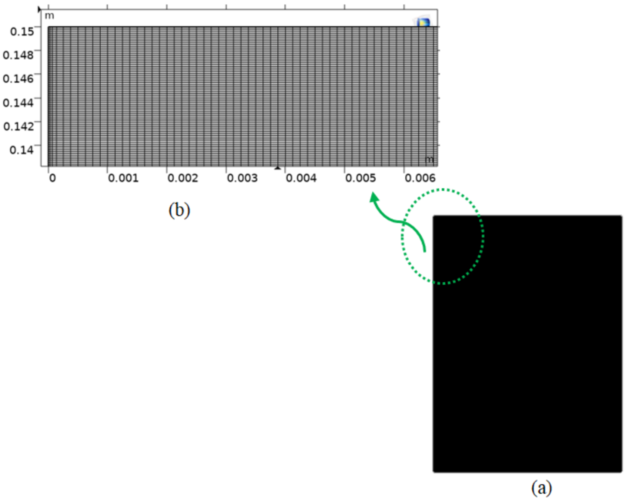

Fig. 9. (a) Fine mesh applied in the model, (b) magnified region of the model.

3.3 Numerical model validation

The model was validated by comparing the simulated polarization curve with the COMSOL Multiphysics report [44]. Polarization curves serve as a crucial tool for characterizing the electrochemical performance of an electrolyzer cell, illustrating the relationship between the applied voltage and the resulting current density. These curves are essential for identifying the cell's operational voltage and current conditions. As the current density increases, the rate of gas evolution at the electrode surfaces also rises, leading to the formation of more gas bubbles – primarily hydrogen at the cathode and oxygen at the anode. These gas bubbles increase the resistance within the electrolyte by reducing its electrical conductivity, which in turn contributes to a rise in cell voltage. In the reference geometry, the anode and cathode measured 2 mm × 100 mm, while the separator measured 1 mm × 100 mm. The maximum hydrogen volume fraction was recorded at 0.35, with hydrogen bubbles accumulating more densely near the top of the electrode. The polarization curve data from the reference and benchmark models were recorded and compared. Figure 10 illustrates the model validation, demonstrating that the difference between the results was less than 2%.

4 Results and Discussions

4.1 Selection of optimized renewable energy

If residential energy demand were met solely by grid electricity, the system's NPC would amount to

$2,024,255.18. The annual operational and maintenance expenses were estimated at $156,585, with the grid electricity rate of $0.143/kWh. In this scenario, no capital expenditure was incurred, as no new infrastructure or equipment investment was required. The system relies entirely on the existing grid, eliminating the upfront costs typically associated with renewable or hybrid energy systems. The financial key performance indicator (KPI) is presented in Figure 11. The total CO_2 emissions from this system were recorded at 692,040 kg/yr, a significant amount due to the grid's reliance on a diverse energy mix that includes both renewable sources and fossil fuels. Figure 11 provides a summary of the financial KPIs for the system using grid electricity.

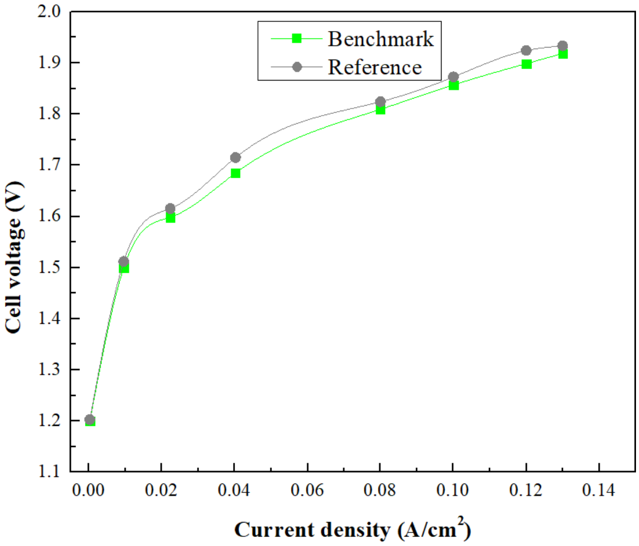

Fig. 10. Comparison of cell voltage variation versus current density with the data obtained from [44].

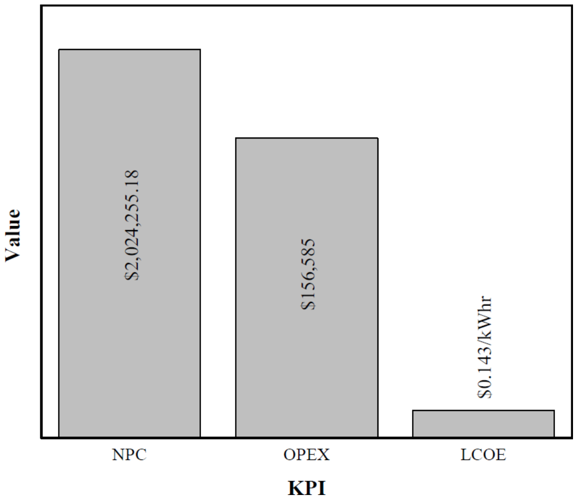

Fig. 11. Financial KPI of the system using grid electricity.

Using the cost multiplier as a sensitivity parameter, the HOMER Pro optimizer determined that a hybrid system could optimize energy sources to meet residential demand based on financial KPIs. The cost multiplier for each component – solar PV, system converter, and wind turbine – was increased by 20%, while the grid electricity rate was analyzed at $0.143/kWh and $0.150/kWh. Considering the lowest financial KPIs and the highest renewable energy fraction, the optimized results identified a combination of solar, wind, and grid electricity as the most effective solution.

A combination of a 9 kW wind turbine capacity and grid electricity can generate electricity at a rate of $0.145/kWh. The financial KPIs are presented in Figure 12. The system's NPC, operational expenditure (OPEX), and capital expenditure (CAPEX) were recorded at $2,053,436.62, $1,988,025.81, and $59,400, respectively. The renewable energy fraction from this system was 2.20%, indicating that this configuration does not offer long-term cost-effectiveness. The low renewable energy fraction resulted in a substantial amount of CO_2 emissions, totaling 676,790 kg/year. No excess electricity was generated by this system, which did not meet the objective of this study – producing hydrogen from the excess electricity of the optimized system. Additionally, the LCOE was 1.4% higher than the grid electricity rate, which directly affects hydrogen production costs. This increase in costs is attributed to the higher CAPEX and OPEX for the wind turbines, which led to a rise in both the NPC and LCOE, making the model a less cost-effective option.

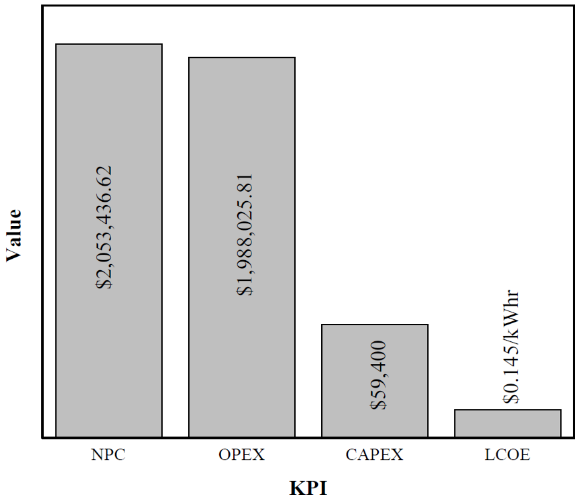

Fig. 12. Wind turbine and grid system's financial KPI.

The combination of a 1000 kW solar PV capacity, a system converter with a 480 kW capacity, and grid electricity can generate electricity at a rate of $0.09/kWh. The financial KPIs are shown in Figure 13. The solar

PV and grid system achieved a renewable energy fraction of 72.8%, indicating that a significant portion of the energy demand was met through renewable sources. Furthermore, the system generated an excess of 438,076 kWh per year, which could be effectively used for hydrogen production. The system's CO_2 emissions were recorded at 207,047 kg/year. However, with a solar PV capacity of 1000 kW, the system is not suitable for residential applications due to its size, exceeding the spatial constraints of typical residential environments.

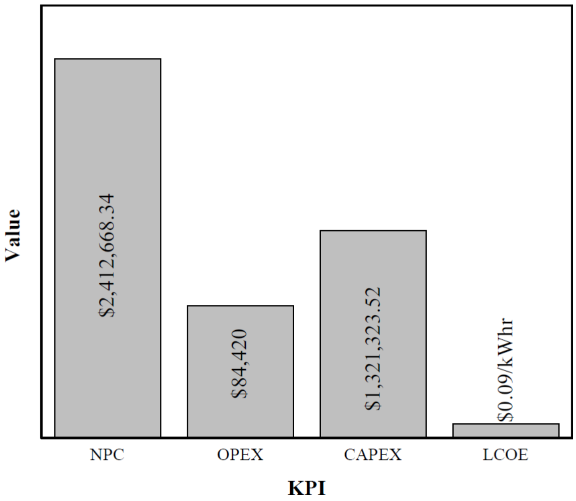

Fig. 13. Solar PV and grid system's financial KPI.

An analysis of Figure 3 and Figure 5 shows that solar and wind energy sources have complementary characteristics within the specific region. By integrating both energy sources, the system ensures a continuous energy supply throughout the year, minimizing the risk of underproduction during periods when one resource is less available. For this reason, the optimization model incorporates solar PV, wind turbines, and grid electricity to improve system reliability and guarantee year-round energy provision. Among the various optimization results, three hybrid systems were selected based on NPC, LCOE, renewable fraction, and excess electricity, which could meet the ultimate objectives of this study and help identify the best option. Table 3 presents the optimized models and their specifications. It is worth noting that the solar PV capacity is higher than that of the system converter because peak solar irradiation occurs over a short period each day and exhibits seasonal variations. These factors contribute to the under-sizing of the system converter.

Figure 14 presents the KPIs for the three optimized models (OM1, OM2, and OM3). The NPC of OM1 is 4% lower than that of OM2 and 7% lower than OM3, primarily due to OM1's lower CAPEX, which is over 2% lower than OM2 and 32% lower than OM3. This difference is largely attributed to the higher cost of wind turbines in OM2 and OM3, as their capacities are significantly larger than in OM1. Specifically, OM1 includes a wind turbine capacity of only 6 kW, whereas OM2 and OM3 feature capacities of 17 kW and 45 kW, respectively. The increased wind turbine capacity in OM2 and OM3 results in higher CAPEX, which ultimately raises the overall NPC of the system. OM1's lower CAPEX provides a financial advantage by reducing the NPC, representing the total cost over the project's lifespan. NPC is a crucial KPI for assessing the long-term financial viability of a project. A lower NPC translates to a higher return on investment (ROI) and internal rate of return (IRR), making the system more appealing to investors. The LCOE for OM1 was calculated at \$0.121/kWh, which is over 15% lower than the cost of grid electricity and 6% lower than OM3. This substantial reduction in LCOE makes OM1 the most favorable option for cost-effective hydrogen production within this system. OM1 demonstrated a superior ROI (6.7%) and IRR (9.8%) compared to OM2 and OM3, indicating stronger financial performance. These higher profitability indicators suggest that OM1 presents a more attractive investment opportunity and greater potential for securing funding. ROI and IRR are critical metrics for evaluating the financial feasibility of a project, and OM1's advantage in these areas reinforces its economic viability. However, OM2 produced 103,695 kWh of excess electricity annually, which was over 80% greater than OM1 and more than three times higher than OM3. This difference is attributed to OM2's larger combined solar PV and wind turbine capacity compared to OM1. Although OM3 had a higher wind turbine capacity than OM2, its solar PV capacity (281 kW) was lower than OM2 (368 kW), affecting the overall balance of renewable energy generation. The renewable energy fractions for OM1, OM2, and OM3 were 44.9%, 50.9%, and 50.7%, respectively. While OM2 and OM3 generated over half of their energy from renewable sources – enhancing sustainability – this higher reliance on renewables also contributed to increased system costs. Despite OM2's advantages in excess electricity production and renewable energy fraction, OM1 stands out as the most cost-effective and economically viable solution, with superior financial KPIs, including NPC, LCOE, ROI, and IRR.

The monthly electricity generation from OM1 and its respective energy sources are illustrated in Figure 15. Grid electricity accounted for 50.9% of the total generation, while solar PV contributed 47.8%, making it the dominant renewable energy source. In contrast, wind energy accounted for only 1.27% of the total output. This disparity is largely due to Alberta's higher solar energy potential compared to wind energy.

The inclusion of a wind turbine in OM1 was a strategic decision to mitigate energy demand uncertainties, allowing wind power to supplement the load during periods of solar generation fluctuation. Despite its relatively small share, wind energy enhances the system's resilience and reliability. With nearly half (49.1%) of its electricity derived from renewable sources, OM1 demonstrates strong potential for renewable energy generation. This significantly reduces reliance on non-renewable energy, potentially lowering greenhouse gas emissions and improving the system's environmental footprint. The high renewable energy contribution reinforces OM1's role in advancing energy sustainability, supporting renewable energy targets, and promoting energy independence.

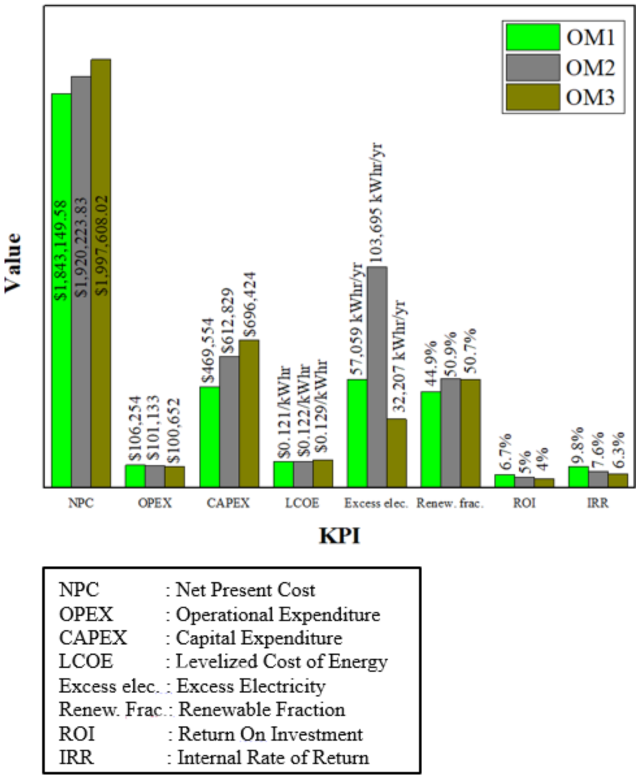

Fig. 14. KPI comparison of three optimized models.

Figure 16 illustrates the net energy purchases for OM1 over the year, with a peak observed in June. The increased energy sold back to the grid during certain months contributed to a reduction in overall energy costs. The lowest recorded energy charge occurred in September, totaling $4,835, while the annual energy cost for the system was $88,574. The sell-back price to the grid was set at $0.05/kWh. If this rate were to increase, the system's net energy cost would decline further, enhancing its financial attractiveness to investors. Additionally, increasing the renewable energy fraction would reduce reliance on grid electricity, further stabilizing long-term energy costs and mitigating the impact of market price fluctuations. By minimizing grid dependency, OM1 can offer greater financial stability and sustainability, making it a more viable and cost-effective energy solution for the future.

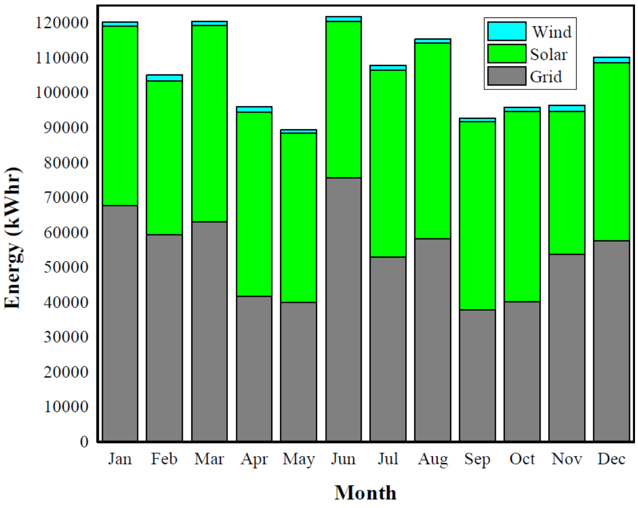

Fig. 15. Monthly energy productions using wind, solar, and grid by OM1.

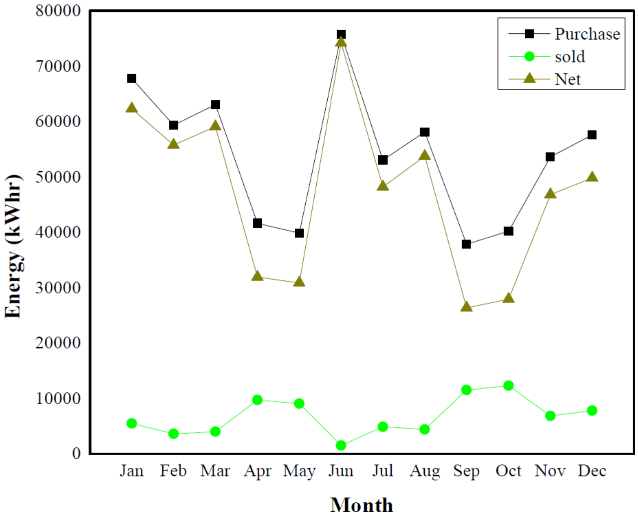

Fig. 16. Net, sold, and purchased energy distributions of OM1 throughout the year.

Figure 16a illustrates the annual solar PV power output of OM1, highlighting seasonal and daily variations. The rated capacity of solar PV was 309 kW, while the mean output reached 345 kW. The highest power generation occurred during the summer months and peaked around midday throughout the year. The system operated for a total of 4,376 hours annually, achieving a PV penetration rate of 55.5%, meaning solar PV met more than half of the total energy demand.

The average daily solar output was 1,665 kWh, with a capacity factor of 22.5%, which is within a favorable range [47]. However, this factor is influenced by sunlight availability, system efficiency, and Alberta's local weather conditions. The LCOE for solar PV was $0.063/kWh, making it a highly cost-effective energy source. This low LCOE significantly reduces overall electricity costs within the hybrid system, enhancing its financial viability and long-term sustainability. By integrating solar PV at a competitive cost, the system achieves greater affordability and efficiency, reinforcing its role as a practical and scalable renewable energy solution. Additionally, the economic benefits of solar PV, coupled with its high renewable energy fraction, contribute to reduced dependence on grid electricity, further decreasing energy costs and minimizing environmental impact.

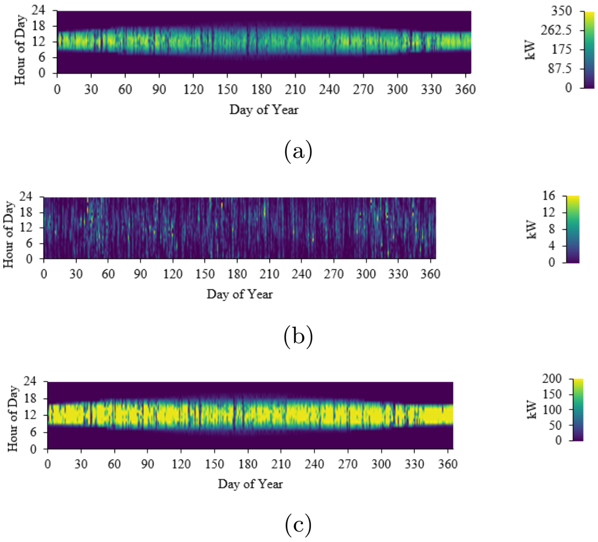

(a)

(b)

(c)

Fig. 17. (a) Solar PV power output of OM1, (b) Power output of wind turbine of OM1, (c) Power output of system converter of OM1.

Figure 16b illustrates the wind turbine power output, which generated 16,086 kWh annually with a total operational time of 6,994 hours. The mean and maximum outputs were 1.84 kW and 15.7 kW, respectively. However, wind penetration was just 1.47%, significantly lower than solar penetration. The levelized cost of wind energy was $0.237/kWh, 65% higher than the prevailing grid electricity rate, contributing to the hybrid system's overall LCOE of $0.121/kWh. This higher cost reduced the system's economic efficiency. While wind energy contributes to the diversification of energy sources within the hybrid system, its relatively low penetration and higher cost make it less economically competitive compared to solar PV. However, incorporating wind energy still plays a role in enhancing system reliability and resilience, mitigating risks associated with fluctuations in solar generation. A more cost-effective wind power contribution could have further lowered the LCOE, enhancing the system's financial viability. Despite its higher cost, the wind turbine was integrated into OM1 to address energy uncertainties and weather variability, ensuring a more resilient and reliable energy supply.

Figure 16c illustrates the power output of the system converter, with a mean output of 58.5 kW and a maximum output of 194 kW. The capacity factor was 30.2%, which would decrease if a higher-capacity converter were selected. The system converter generated 512,090 kWh annually, operating for 4,376 hours, aligning with the operational time of the solar PV system. Energy losses were recorded at 7%, primarily due to switching losses in power electronics, which are inherent to the conversion process and contribute to overall efficiency reductions.

The renewable penetration of the system reached 53%, which is defined as the ratio of total renewable generation to total load. This highlights the system's significant reliance on renewable energy, contributing to lower emissions and enhanced grid stability. Total CO_2 emissions from OM1 were recorded at 358,233 kg per year, primarily due to grid electricity consumption, which includes a mix of renewable and non-renewable sources.

The excess electricity from OM1 accounted for 4.49% of its total production, totaling 57,059 kWh per year. The system successfully met all electric load demands, ensuring no shortages through adequate generation and storage. With an LCOE of $0.121/kWh, this surplus electricity presents a cost-effective opportunity for green hydrogen production. Assuming a water electrolyzer efficiency of 70%, the available energy for hydrogen production would be 39,941 kWh. Given that hydrogen's lower heating value is 242,000 kJ/kg-mol, this surplus energy could generate approximately 1,188 kg of hydrogen annually. Strategically integrating electrolysis into the system enhances economic viability and environmental sustainability, making it a practical step toward a cleaner energy transition.

4.2 Numerical simulation for hydrogen production from water electrolysis

In the model, the key parameters selected were the distance between the electrode and separator, as well as the height of the gas compartments. Figure 18 shows the hydrogen production, represented by the volume fraction, at different heights of the hydrogen compartment. Hydrogen production was lowest at the bottom of the electrode, with an increasing trend observed as measurements were taken higher along the electrode, reaching a peak at the top. This can be attributed to gas accumulation and flow rate dynamics, as the highest gas concentration is recorded at the top of the electrode [33]. However, the error percentage between the model and reference was more than 20%, which could be attributed to the distance between the electrode and separator being crucial for hydrogen production. Increasing this distance will eventually reduce hydrogen production. This could be due to the increase in the electrolyte volume between the electrode and the separator, which in turn increases the overall resistance of the system. The higher resistance impedes the efficient flow of current, reducing hydrogen production.

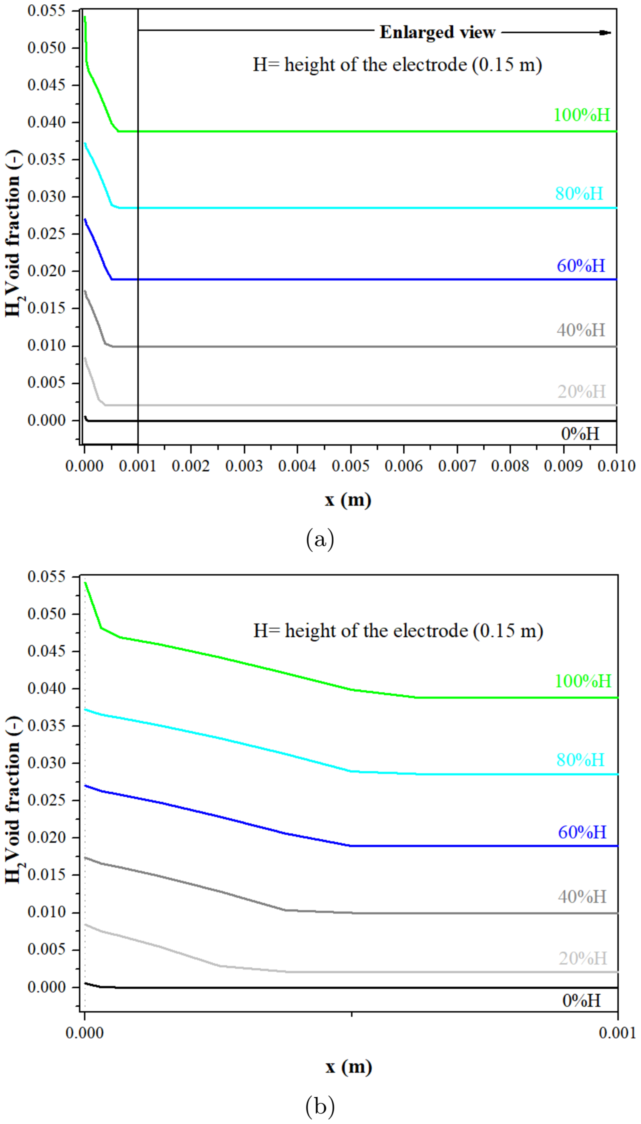

Fig. 18. Hydrogen volume fraction distributions at different heights of (a) the electrode and (b) an enlarged view near the electrode surface.

The dispersed phase volume fraction diagram shown in Figure 19 illustrates the volume fraction of the dispersed phase, representing the proportion of the total volume occupied by hydrogen gas at each point within the domain, which was monitored over time. Results indicated that the volume fraction was 0.035 after 1 minute, increased to 0.12 after 3 minutes, and reached 0.2 after 5 minutes. The governing equations confirmed the study as time-dependent, as variables changed over time, and this change was observed for 5 minutes. It seemed that ohmic losses increased due to the distance between the electrode and the separator being 0.01 m. A shorter distance would typically require less electrolyte, reducing ohmic losses [33]. However, assuming the flow regime was laminar, it was initially believed that the distance between the electrode and diaphragm would not significantly impact hydrogen production. In reality, the increased distance between the electrode and separator does have a substantial effect on reaction kinetics. A larger gap introduces more electrolyte between the electrodes, which increases the ohmic resistance, thereby affecting the efficiency of the reaction. Higher resistance impedes the movement of ions, which slows down the electrochemical reactions. The slower reaction kinetics lead to decreased hydrogen production. The reduction in the hydrogen volume fraction is primarily attributed to ohmic losses. A larger separation between the electrode and separator allows for more electrolyte in the gap, which increases the ionic conduction path, leading to higher resistive losses. This highlights the critical role of minimizing the electrode-electrolyte distance to reduce ohmic resistance and maintain efficient hydrogen production. However, the efficiency of zero-gap electrolyzers may decrease significantly at high current densities, as the generated gases hinder electrolyte flow and the electrode reactions [48].

The velocity magnitude in the continuous phase is shown in Figure 19. After 1 and 3 minutes, the maximum velocity magnitude was recorded at 0.15 m/s, while after 5 minutes, it increased to 0.2 m/s. The regions with the highest hydrogen void fraction coincided with areas of maximum velocity. This behavior can be attributed to the dynamics of multiphase flow, where the interaction between the gas and liquid phases is strongly influenced by localized resistance. In areas with lower resistance, typically caused by higher gas-phase concentrations (i.e., hydrogen void fraction), the fluid moves more freely. This reduced resistance facilitates the velocity of both the liquid electrolyte and the hydrogen gas bubbles. The interphase momentum transfer is represented in Figure 19. Babay et al. demonstrated that increasing the concentration of KOH in the electrolyte enhances interphase momentum transfer, resulting in more vigorous gas evolution and the formation of larger gas bubbles [49]. In this study KOH concentration was kept at 6.1 mol/m^3. The interphase momentum transfer was recorded at 20 N/m^3 after 1 minute, increased to 200 N/m^3 after 3 minutes, and reached 500 N/m^3 after 5 minutes. It seemed that the interphase momentum transfer profile also closely aligns with the gas volume fraction distribution. In regions where the gas volume fraction is higher, interphase momentum transfer is also increased. This suggests a direct relationship between the intensity of gas production and the momentum exchange between the phases. Additionally, it was observed that a larger gap between the electrode and the separator negatively affects reaction kinetics, resulting in reduced interphase momentum transfer away from the electrode surface.

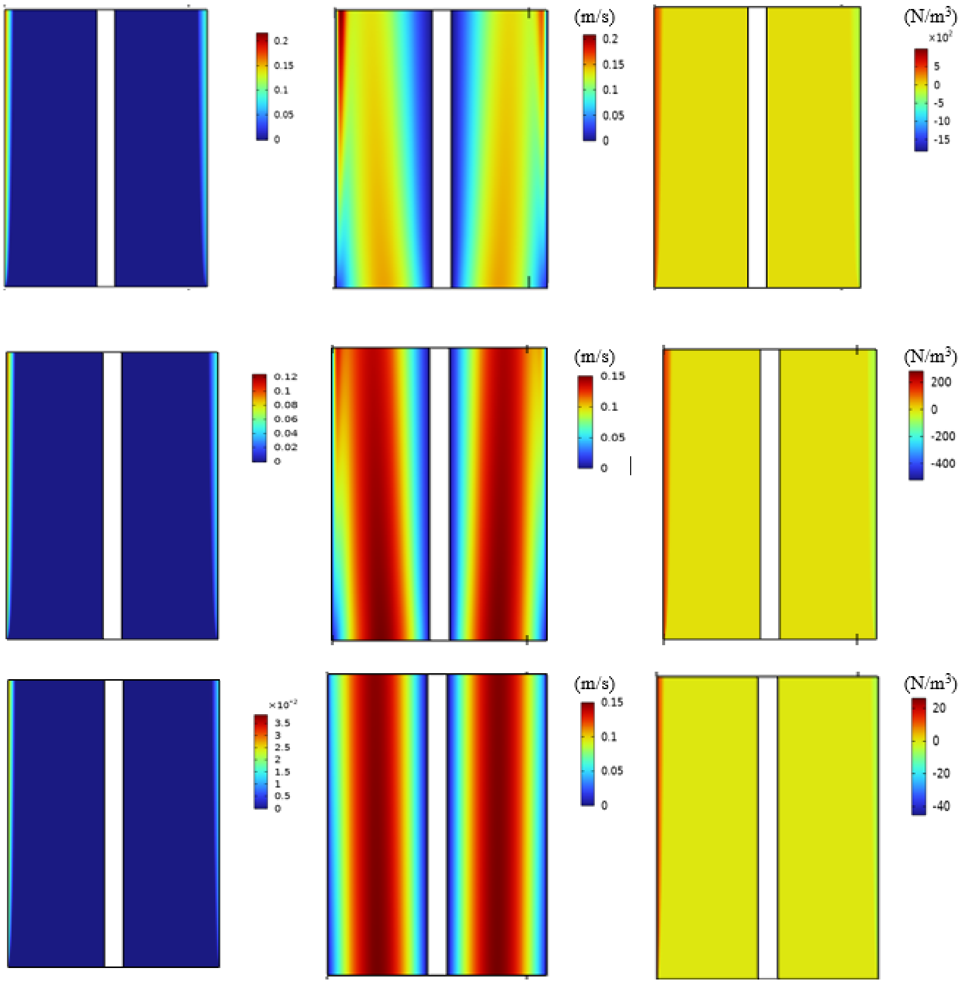

Fig. 19. Distributions of gas volume fraction in the dispersed phase (left column), velocity magnitude in the continuous phase (middle column), and interphase momentum transfer (right column) at $t_1 = 5\,\text{min}$ (top row), $t_2 = 3\,\text{min}$ (middle row), and $t_3 = 1\,\text{min}$ (bottom row).

The polarization curves at various temperatures were presented in Figure 20. The results demonstrated that increasing the temperature enhances the reaction kinetics, resulting in a noticeable reduction in cell potential. This decrease in cell potential signifies enhanced efficiency in the electrochemical process, as less energy is required to drive the reaction at higher temperatures. The improved kinetics are attributed to the accelerated ion transport rates and the reduced activation barriers for electrochemical reactions. This trend is consistent with findings from previous studies, reinforcing the well-established correlation between elevated temperatures and improved electrolysis performance [33].

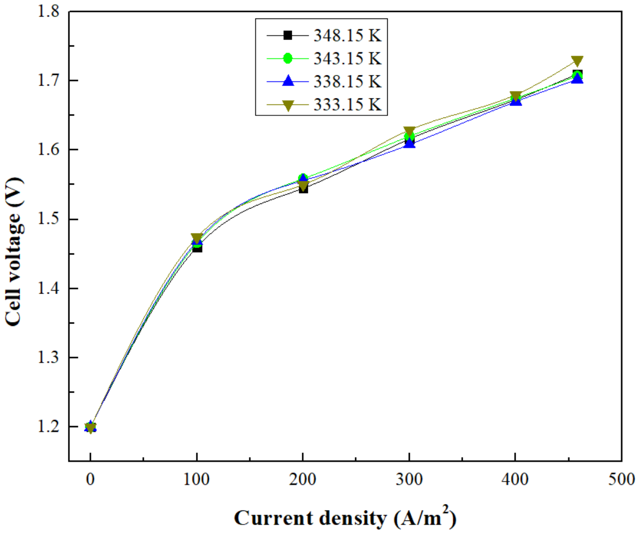

Fig. 20. Polarization curve at different temperatures, which represents the cell voltage as a function of current density.

The volume force refers to the forces acting on the gas phase dispersed within the liquid electrolyte, such as buoyancy and gravitational forces. These forces govern the motion and behavior of gas bubbles during the electrolysis process. The highest void fraction generation was observed near the top of the electrode. Consequently, the volume force was evaluated at two specific heights along the electrode: 150 mm and 120 mm, as shown in Figure 21. At the 150 mm height, the maximum volume force in the dispersed phase was measured at 1706 N/m^3 near the cathode wall, rapidly decreasing in magnitude as the distance from the electrode surface increased. In contrast, at the 120 mm height, the peak volume force was recorded at 284 N/m^3, occurring 0.375 mm away from the cathode wall. This variation in volume force across the electrode height and proximity to the wall highlights the spatial distribution of the forces acting on the gas bubbles. These forces are closely linked to the generation and transport of the dispersed phase within the electrolyte, influencing the overall dynamics of bubble movement and gas evolution during the electrolysis process.

The mid-separator current density at different heights of the electrode is shown in Figure 22, ranging from 453 to 440 A/m^2. This is in contrast to the COMSOL Multiphysics report [44], where the mid-separator current density ranges from 1300 to 1155 A/m^2. The relatively consistent mid-separator current density observed in this study promotes stable hydrogen generation, which in turn contributes to increased system efficiency [50]. A stable current density across the mid-separator is crucial for maintaining consistent hydrogen production. This uniform current distribution ensures that electrochemical reactions take place evenly throughout the system, promoting reliable performance. Additionally, a steady current density helps prevent localized regions of excessive heat or concentration gradients, which could lead to energy losses or operational instability. By maintaining this uniformity, the system enhances the efficient conversion of electrical energy into chemical energy, optimizing hydrogen production while minimizing energy waste.

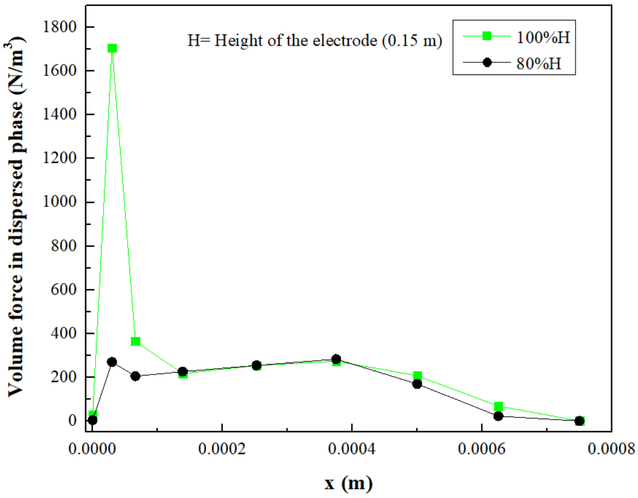

Fig. 21. Volume force in dispersed phase at heights of electrode.

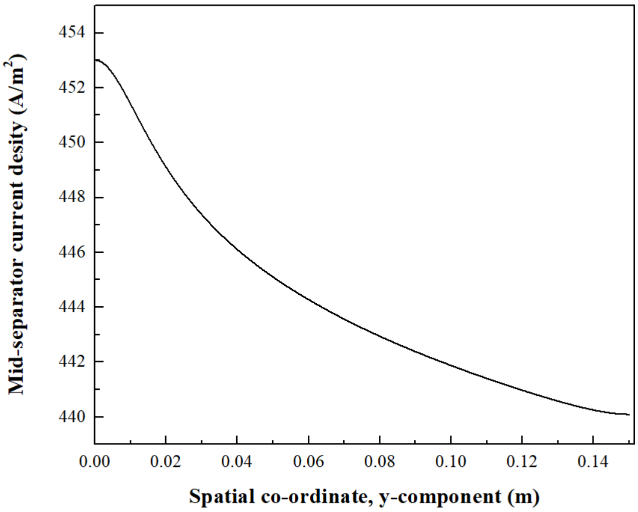

Fig. 22. Spatial co-ordinate distribution of mid-separator current density at a cell voltage of 1.2 V.

4.3 Limitations of CFD assumptions

This study specifically focuses on the design considerations for residential electrical loads, aiming to optimize energy use and integrate renewable energy sources for hydrogen production at the household level. While the findings provide valuable insights into residential-scale applications, their scalability to larger or industrial-scale systems is beyond the scope of this research. Future studies could explore the adaptation of the proposed methods and designs to industrial contexts, addressing unique challenges such as higher energy demands, increased system complexity, and economic feasibility at scale.

Additionally, certain assumptions in the CFD simulations, such as Newtonian and laminar flow, may limit the applicability of the results to real-world scenarios. For instance, transitions from laminar to turbulent flow could lead to inaccuracies when predicting the hydrogen gas volume fraction within the dispersed phase. Moreover, in the polarization curve, variations in voltage drops and current density could occur due to changes in reaction kinetics. This highlights the need for experimental validation and more comprehensive modeling approaches to address these limitations.

5 Conclusion

In this study, renewable energy sources for Alberta were selected based on optimization results from HOMER Pro, focusing on residential loads. The analysis showed that a combination of Solar PV, wind turbines, and grid power (OM1) could deliver electricity at a competitive rate of \$0.121/kWh. Financial indicators for OM1, including net present cost, return on investment, and internal rate of return, were calculated to be \$1.84 million, 6.7%, and 9.8%, respectively, making it an attractive option for potential investors. Additionally, OM1 generated surplus electricity of 57,059 kWh per year, which can be used for water electrolysis to produce an estimated 1,188 kg of green hydrogen, thereby lowering hydrogen production costs. CFD simulations emphasized the effect of increasing the distance between the electrode and the separator, which significantly reduced the hydrogen volume fraction, resulting in a model-to-reference error greater than 20%. The peak hydrogen gas volume fraction (0.2) was observed in the upper region of the cathode after 5 minutes, attributed to gas accumulation and flow rate dynamics. Regions with the highest gas volume fraction coincided with areas of maximum velocity magnitudes and interphase momentum transfer. Additionally, the maximum volumetric force, recorded at 1706 N/m^3, was found in the same region. The polarization curve indicated that elevated temperatures enhanced reaction kinetics, leading to a reduction in cell voltage. A lower cell voltage improves cell efficiency, decreasing the energy required for operation. However, an interesting insight emerged during the analysis of mid-separator current density. The model showed a variation in current density between 453 A/m^2 and 440 A/m^2, suggesting that maintaining a consistent current density not only enhances cell efficiency but also minimizes electrode wear and tear, ensuring stable hydrogen production. These findings are crucial for identifying the optimal operating conditions within the laminar flow regime to achieve efficient hydrogen production. Future electrolyzer designs should focus on maintaining a consistent current density across the mid-separator region to ensure uniform performance and maximize efficiency. Further studies in this area would offer valuable insights into real-world performance, operational challenges, and potential improvements for the proposed design.

References

[1] Zhong Q, Zhang Z, Wang H, Zhang X, Wang Y, Wang P, et al. Incorporating scarcity into footprints reveals diverse supply chain hotspots for global fossil fuel management. Applied Energy. 2023;349:121692.

[2] Alagoz E, Alghawı Y. The future of fossil fuels: challenges and opportunities in a low-carbon. International Journal of Earth Sciences Knowledge and Applications. 2024;5(3):381–388.

[3] Londoño-Pulgarin D, Cardona-Montoya G, Restrepo JC, Muñoz-Leiva F. Fossil or bioenergy? Global fuel market trends. Renewable and Sustainable Energy Reviews. 2021;143:110905.

[4] Ou J, Liu X, Li X, Shi X. Mapping global fossil fuel combustion CO 2 emissions at high resolution by integrating nightlight, population density, and traffic network data. IEEE Journal of Selected Topics in Applied Earth Observations and Remote Sensing. 2015;9(4):1674–1684.

[5] Hunt ND, Liebman M, Thakrar SK, Hill JD. Fossil energy use, climate change impacts, and air quality-related human health damages of conventional and diversified cropping systems in Iowa, USA. Environmental science & technology. 2020;54(18):11002–11014.

[6] Solomon CG, Salas RN, Malina D, Sacks CA, Hardin CC, Prewitt E, et al.. Fossil-fuel pollution and climate change—a new NEJM group series. Massachusetts Medical Society; 2022.

[7] Habib-ur Rahman M, Ahmad A, Raza A, Hasnain MU, Alharby HF, Alzahrani YM, et al. Impact of

climate change on agricultural production; Issues, challenges, and opportunities in Asia. Frontiers in Plant Science. 2022;13:925548.

[8] Elavarasan RM, Shafiullah G, Padmanaban S, Kumar NM, Annam A, Vetrichelvan AM, et al. A comprehensive review on renewable energy development, challenges, and policies of leading Indian states with an international perspective. Ieee Access. 2020;8:74432–74457.

[9] Shoaib A, Ariaratnam S. A study of socioeconomic impacts of renewable energy projects in Afghanistan. Procedia Engineering. 2016;145:995–1003.

[10] Mazloomi K, Gomes C. Hydrogen as an energy carrier: Prospects and challenges. Renewable and sustainable energy reviews. 2012;16(5):3024–3033.

[11] Amin M, Shah HH, Fareed AG, Khan WU, Chung E, Zia A, et al. Hydrogen production through renewable and non-renewable energy processes and their impact on climate change. International journal of hydrogen energy. 2022;47(77):33112–33134.

[12] Majewski P, Salehi F, Xing K. Green hydrogen. AIMS Energy. 2023;11(5):878–895.

[13] El-Shafie M. Hydrogen production by water electrolysis technologies: A review. Results in Engineering. 2023;20:101426.

[14] Santos DM, Sequeira CA, Figueiredo JL. Hydrogen production by alkaline water electrolysis. Química Nova. 2013;36:1176–1193.

[15] Tashie-Lewis BC, Nnabuife SG. Hydrogen Production, Distribution, Storage and Power Conversion in a Hydrogen Economy - A Technology Review. Chemical Engineering Journal Advances. 2021;8:100172. Available from: https://www.sciencedirect.com/science/article/pii/S2666821121000880.

[16] Sebbahi S, Nabil N, Alaoui-Belghiti A, Laasri S, Rachidi S, Hajjaji A. Assessment of the three most developed water electrolysis technologies: alkaline water electrolysis, proton exchange membrane and solid-oxide electrolysis. Materials Today: Proceedings. 2022;66:140–145.

[17] Hodges A, Hoang AL, Tsekouras G, Wagner K, Lee CY, Swiegers GF, et al. A high-performance capillary-fed electrolysis cell promises more cost-competitive renewable hydrogen. Nature communications. 2022;13(1):1304.

[18] Cho HH, Strezov V, Evans TJ. Environmental impact assessment of hydrogen production via steam methane reforming based on emissions data. Energy Reports. 2022;8:13585–13595.

[19] Ji M, Wang J. Review and comparison of various hydrogen production methods based on costs and life cycle impact assessment indicators. International Journal of Hydrogen Energy. 2021;46(78):38612–38635.

[20] Sorgulu F, Dincer I. Cost evaluation of two potential nuclear power plants for hydrogen production. International Journal of Hydrogen Energy. 2018;43(23):10522–10529.

[21] Constantin A. Nuclear hydrogen projects to support clean energy transition: Updates on international initiatives and IAEA activities. International Journal of Hydrogen Energy. 2024;54:768–779.

[22] Nikolaidis P, Poullikkas A. A comparative overview of hydrogen production processes. Renewable and sustainable energy reviews. 2017;67:597–611.

[23] Bartels JR, Pate MB, Olson NK. An economic survey of hydrogen production from conventional and alternative energy sources. International journal of hydrogen energy. 2010;35(16):8371–8384.

[24] Herdem MS, Mazzeo D, Matera N, Baglivo C, Khan N, Congedo PM, et al. A brief overview of solar and wind-based green hydrogen production systems: Trends and standardization. International Journal of Hydrogen Energy. 2024;51:340–353.

[25] Yilmaz C. Optimum energy evaluation and life cycle cost assessment of a hydrogen liquefaction system assisted by geothermal energy. International Journal of Hydrogen Energy. 2020;45(5):3558–3568.

[26] Chidire A, Schifflechner C, Massier T. Life cycle assessment of green hydrogen production via

geothermal energy-driven electrolysis. In: 2023 IEEE PES Innovative Smart Grid Technologies-Asia (ISGT Asia). IEEE; 2023. p. 1–5.

[27] Zeng K, Zhang D. Recent progress in alkaline water electrolysis for hydrogen production and applications. Progress in energy and combustion science. 2010;36(3):307–326.

[28] Rahmat MAA, Abd Hamid AS, Lu Y, Ishak MAA, Suheel SZ, Fazlizan A, et al. An analysis of renewable energy technology integration investments in Malaysia using HOMER pro. Sustainability. 2022;14(20):13684.

[29] Khalil L, Bhatti KL, Awan MAI, Riaz M, Khalil K, Alwaz N. Optimization and designing of hybrid power system using HOMER pro. Materials Today: Proceedings. 2021;47:S110–S115.

[30] Asghar F, Hussain MI, Alshahrani FA, Akhtar MI, Amjad W, Shahzad M, et al. Technoeconomic analysis of standalone hybrid renewable energy systems for telecommunication sector under different climatic conditions in Saudi Arabia. Energy Reports. 2024;11:4067–4084.

[31] Achour Y, Berrada A, Arechkik A, El Mrabet R. Techno-Economic Assessment of hydrogen production from three different solar photovoltaic technologies. International Journal of Hydrogen Energy. 2023;48(83):32261–32276.

[32] Brauns J, Turek T. Alkaline water electrolysis powered by renewable energy: A review. Processes. 2020;8(2):248.

[33] Rodríguez J, Amores E. CFD modeling and experimental validation of an alkaline water electrolysis cell for hydrogen production. Processes. 2020;8(12):1634.

[34] Upadhyay M, Kim A, Paramanantham SS, Kim H, Lim D, Lee S, et al. Three-dimensional CFD simulation of proton exchange membrane water electrolyser: Performance assessment under different condition. Applied Energy. 2022;306:118016.

[35] Jang D, Cho HS, Lee S, Park M, Kim S, Park H, et al. Investigation of the operation characteristics and optimization of an alkaline water electrolysis system at high temperature and a high current density. Journal of Cleaner Production. 2023;424:138862.

[36] Khodaei M, Darabi Z, Omidifar M, et al. Modeling and simulation of the fluid dynamic and performance of the Pd-based membrane by CFD for hydrogen separation. Hydrogen, Fuel Cell & Energy Storage. 2022;9(1):19–25.

[37] Muhsen H, Alshawabkeh M, Al-Mahmodi M, Ghanem A, Al-Halhouli A. Sensitivity analysis of electrodes spacing media for evaluating alkaline electrolyzer performance through CFD modeling. Renewable Energy Focus. 2024;49:100575.

[38] Arikan Y, Arslan ÖP, Cam E. The analysis of wind data with rayleigh distribution and optimum turbine and cost analysis in Elmadag, Turkey. Istanbul University-Journal of Electrical and Electronics Engineering. 2015;.

[39] Shi H, Dong Z, Xiao N, Huang Q. Wind speed distributions used in wind energy assessment: a review. Frontiers in Energy Research. 2021;9:769920.

[40] Hodge BK. Alternative energy systems and applications. John Wiley & Sons; 2017.

[41] Farret FA, Simões MG. Integration of renewable sources of energy. John Wiley & Sons; 2017.

[42] Xia Y, Gao M, Yu J, Si Y, Chen L, Mei S. Numerical Study on Hydrodynamic Characteristics and Electrochemical Performance of Alkaline Water Electrolyzer by Micro-Nano Surface Electrode. Materials. 2022;15(14):4927.

[43] Mohsin HM, Zhuo Y, Shen Y. Eulerian-Eulerian-VOF multifluid modelling of liquid–gas reacting flow for hydrogen generation in an alkaline water electrolyser. Fuel. 2024;373:132164.

[44] COMSOL Multiphysics 6 0. Alkaline Electrlyzer;. Available from: `https://doc.comsol.com/6.0/doc/com.comsol.help.models.fce.alkaline_electrolyzer/alkaline_electrolyzer.html`.

[45] COMSOL Multiphysics 5 3. Electrochemistry Module;. Available from: `https://doc.comsol.com/5.3/doc/com.comsol.help.echem/ElectrochemistryModuleUsersGuide.pdf`.

[46] Michaelides EE, Sommerfeld M, van Wachem B. Multiphase flows with droplets and particles. CRC Press; 2022.

[47] Boretti A, Castelletto S. Trends in performance factors of large photovoltaic solar plants. Journal of Energy Storage. 2020;30:101506.

[48] Borisov G, Bachvarov V, Rashkov R, Slavcheva E. Advanced alkaline water electrolysis stack with non-noble catalysts and hybrid electrical connections of the single cells. Catalysts. 2024;14(3):179.

[49] Babay MA, Adar M, Chebak A, Mabrouki M. Dynamics of gas generation in porous electrode alkaline electrolysis cells: An investigation and optimization using machine learning. Energies. 2023;16(14):5365.

[50] Dobó Z, Palotás ÁB. Impact of the current fluctuation on the efficiency of alkaline water electrolysis. International Journal of Hydrogen Energy. 2017;42(9):5649–5656.